EurJIC
European Journal of Inorganic Chemistry

Research Article
doi.org/10.1002/ejic.202200596

Chemistry Europe
European Chemical Societies Publishing

www.eurjic.org

Special Collection

Conformational Effects of Regioisomeric Substitution on the Catalytic Activity of Copper/Calix[8]arene C–S Coupling

Armando Berlanga-Vázquez,[a] Radu A. Talmazan,[b] Carlos A. Reyes-Mata,[a] Edmundo G. Percástegui,[c] Marcos Flores-Alamo,[d] Maren Podewitz,*[b] and Ivan Castillo*[a]

Functionalization of the phenolic rim of *p-tert*-butylcalix[8]arene with phenanthroline to create a cavity leads to formation of two regioisomers. Substitution of positions 1 and 5 produces the known C_{2v}-symmetric regioisomer 1,5-(2,9-dimethyl-1,10-phenanthroyl)-*p-tert*-butylcalix[8]arene (**L**^{1,5}), while substitution of positions 1 and 4 produces the C_s-symmetric regioisomer 1,4-(2,9-dimethyl-1,10-phenanthroyl)-*p-tert*-butylcalix[8]arene (**L**^{1,4}) described herein. [**Cu(L**^{1,4}**)I**] was synthesized from **L**^{1,4} and CuI in good yield and characterized spectroscopically. To evaluate the effect of its cavity on catalysis, Ullmann-type C–S coupling was chosen as proof-of-concept. Selected aryl halides were used, and the results compared with the previously reported Cu(I)/**L**^{1,5} system. Only highly activated aryl halides generate the C–S coupling product in moderate yields with the Cu(I)/**L**^{1,4} system. To shed light on these observations, detailed computational investigations were carried out, revealing the influence of the calix[8]arene macrocyclic morphology on the accessible conformations. The **L**^{1,4} regioisomer undergoes a deformation that does not occur with **L**^{1,5}, resulting in an exposed catalytic center, presumably the cause of the low activity of the former system. The 1,4-connectivity was confirmed in the solid-state structure of the byproduct [**Cu(L**^{1,4}**–H)**$(CH_3CN)_2$] that features Cu(I) coordinated inside a cleft defined by the macrocyclic framework.

Introduction

The application of molecules that provide a confined space as catalysts has been the focus of increasing attention in recent years.[1–4] These systems present a cavity as their main feature,[5] where they can host diverse reactants in a chemical environment that may differ significantly from that provided by the bulk solution. In this context, the macrocycles known as calix[n]arenes have been used as nanoreactors for a large range of processes, including as stabilizers for supported molecular noble-metal catalysts,[6] organic transformations,[7–10] small molecule activation,[11–13] as well as C–C[14,15] and C–N[16] cross-coupling reactions. Although the examples cited create a confined environment for the catalytic reaction to proceed, the metal involved is found outside the cavity of the calixarene (*exo*-coordinated). Very few examples of *endo*-coordinated metal complexes exist,[17,18] and even fewer that participate in catalytic transformations.[19] Calixarenes are synthetically available on a large scale and can be functionalized with relative ease.[20] In the specific case of calix[8]arenes that feature eight phenolic moieties, functionalization requires the use of a base, with CsF or Cs_2CO_3 commonly employed due to the additional templating effect of caesium, which allows control of the regioselectivity.[21,22]

Our research group reported the catalytic activity of copper-based calix[8]arene derivatives for C–S cross coupling reactions, with a bridging phenanthroline motif introduced at the 1 and 5 positions of the phenolic rim (**L**^{1,5} in Scheme 1, left). The Cu(I) complex of **L**^{1,5} is very active for C–S coupling compared to molecular analogues, and displays a higher reactivity towards arylbromides, relative to aryliodides. [23] Under the conditions employed to obtain the 1,5-functionalized calix[8]arene, a side-product obtained in low yield from the reaction mixture was suspected to correspond to a regioisomer with different attachment points to the phenolic positions. Modification of the conditions resulted in improved yields of the latter compound that based on the isolated mass, corresponds to an almost 1:1 mixture of **L**^{1,5} and the new product (Scheme 1, right). To investigate the identity and properties of the previously unidentified regioisomer, we herein report the isolation and characterization of the new compound as the 1,4-phenanthroline substituted calix[8]arene (**L**^{1,4}) and the catalytic activity of its Cu(I) complexes in C–S coupling reactions for comparison

[a] *A. Berlanga-Vázquez, C. A. Reyes-Mata, Prof. I. Castillo*
Instituto de Química, Universidad Nacional Autónoma de México
Ciudad Universitaria, 04510, Ciudad de México (México)
E-mail: joseivan@unam.mx
iquimica.unam.mx/dr-ivan-castillo-perez
[b] *R. A. Talmazan, Prof. M. Podewitz*
Institute of Materials Chemistry, TU Wien
Getreidemarkt 9, 1060 Vienna (Austria)
E-mail: maren.podewitz@tuwien.ac.at
www.podewitz-lab.org
[c] *Prof. E. G. Percástegui*
Centro Conjunto de Investigación en Química Sustentable UAEM-UNAM
Carretera Toluca-Atlacomulco km 14.5
Toluca, 50200, Estado de México (México)
[d] *Dr. M. Flores-Alamo*
Facultad de Química, División de Estudios de Posgrado
Universidad Nacional Autónoma de México
Ciudad Universitaria, 04510, Ciudad de México (México)

Supporting information for this article is available on the WWW under https://doi.org/10.1002/ejic.202200596

Part of the Special Collection on "Inorganic Reaction Mechanisms".

Research Article
doi.org/10.1002/ejic.202200596

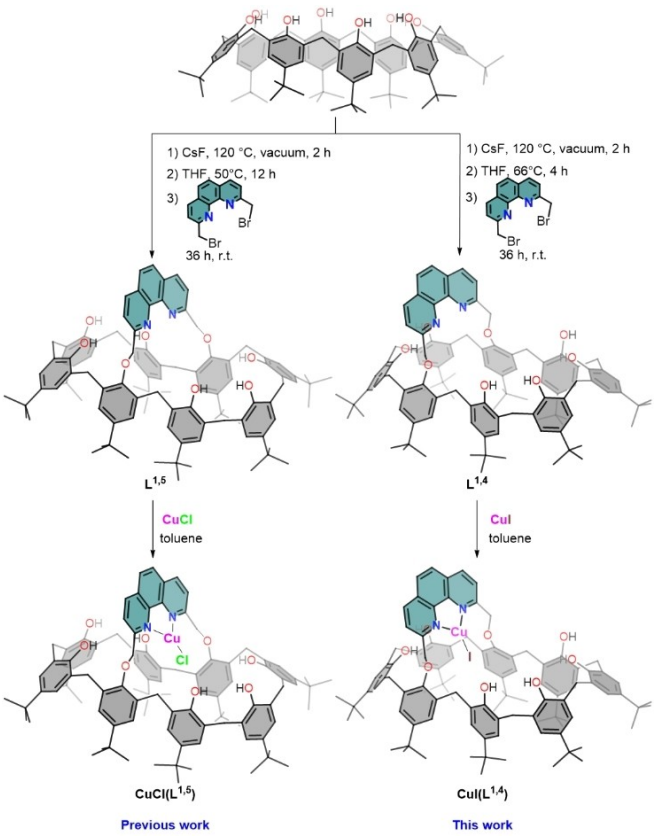

Scheme 1. Synthetic route for [**Cu(L^{1,5})Cl**] (references 23, 25) and [**Cu(L^{1,4})I**] (this work).

with the **L^{1,5}**-based system. The 1,4-substitution pattern may produce significant differences in the properties of the cavity, and concomitantly modify the catalytic activity of its Cu(I) complex. Molecular Dynamics (MD) simulations in explicit solvent, accompanied by Density Functional Theory (DFT) calculations capture the dynamic behavior of the flexible macrocycle and its copper complexes. They revealed that regioisomer-induced conformational changes of the calix[8]arene cavity are likely responsible for the dramatic difference in the catalytic performance of both systems, with the 1,4-regioisomer acting as a poor C–S coupling catalyst. Our studies provide guidance for the future development of better calixarene-based nanoreactors.[24]

Results and Discussion

Synthesis and Characterization

Calixarene derivatives. The functionalization of calix[8]arene with a phenanthroline bridge has previously been reported by our group.[25] In this O-alkylation process, one equivalent of calix[8]arene reacts with 1.2 equivs. of 2,9-bis(bromomethyl)-1,10-phenanthroline in THF in the presence of 10 equivs. of CsF as base and template. Deprotonation at 50 °C overnight leads to 82–86% of the C_{2v}-symmetric regioisomer **L^{1,5}** in the original procedure,[25] which made identification of the small amount of side product unviable. In contrast, heating to reflux temperature (66 °C) for 4 h followed by addition of of 2,9-bis(bromomethyl)-1,10-phenanthroline gives rise to a nearly 1:1 mixture of **L^{1,5}** and **L^{1,4}** (Scheme 1). TLC analysis of the latter reaction mixture with 3:1 hexane/acetone as eluant shows the presence of only two products with very similar R_F (0.225 for **L^{1,5}** and 0.275 for **L^{1,4}**, determined after spectroscopic characterization, Figures S1–S7), making it challenging to separate via column chromatography. Separation of the two isomers involved crystallization from 8:1 $CHCl_3$/toluene mixture and cooling to −30 °C of the caesium complexes formed in the presence of excess CsF during alkylation with 2,9-bis(bromomethyl)-1,10-phenanthroline, resulting in the solid identified previously as [**Cs(L^{1,5}–H)**] as a white crystalline solid.[25] Separate treatment of [**Cs(L^{1,5}–H)**] dissolved in CH_2Cl_2, and the pale-yellow mother liquor containing [**Cs(L^{1,4}–H)**] with 0.1 N HCl each afforded the pure **L^{1,5}** and **L^{1,4}**, assessed initially by TLC analysis. The previously unidentified **L^{1,4}** was characterized by MALDI-TOF MS, with a peak at $m/z = 1501.7$ corresponding to the molecular ion (Figure S3). ^{1}H NMR spectroscopic analysis of **L^{1,4}** was undertaken in $C_2D_2Cl_4$ solution, since this solvent results in better resolved peaks for **L^{1,5}**.[23] Noticeable differences include the number of signals arising from the methylene protons of the calixarene framework: the less symmetric **L^{1,4}** should give rise to 5 doublets detected as broad peaks likely due to fluxional processes (Figure S4, see also theoretical section). For comparison, **L^{1,5}** displays only a pair of 1:1 signals due to the symmetry plane defined by the phenanthroline moiety that includes the O-atoms in 1 and 5 positions (Figure S5). The flexibility of macrocyclic **L^{1,4}** is also reflected in the poorly resolved ^{13}C NMR spectrum (Figure S6). The signals sharpen in ^{1}H NMR data acquired at higher temperature, but they do not coalesce completely up to 120 °C (Figures S7-S8).

Copper complexes. Once isolation and identification of **L^{1,4}** was achieved, the corresponding Cu(I) complex was obtained upon treatment of a toluene solution of the macrocycle with a stoichiometric amount of copper iodide dissolved in a minimum amount of acetonitrile under inert atmosphere. Cooling to −30 °C resulted in a brown microcrystalline solid in 82% yield, formulated as **[Cu(L^{1,4})I]** (see below). The IR spectrum evidences a negligible displacement of the C–N band after Cu(I) complexation at 1591 cm^{-1}, relative to the free ligand at 1594 cm^{-1} (Figures S1 and S2).[33] Characterization by ^{1}H NMR spectroscopy confirms that the complex is diamagnetic, as expected for a Cu(I) d^{10} center (Figures S5 and S8). The apparent flexibility of the ligand in solution is restricted upon Cu(I) coordination; this can be discerned in the methylene group signals, as they get resolved into seven doublets with close to 1:1:1:1:1:1:2 ratio at room temperature in $C_2D_2Cl_4$ (Figures S8). MALDI-TOF MS of the complex obtained in acetonitrile solution shows a peak at $m/z = 1503.6$ corresponding to protonated $[L^{1,4}+H]^+$, and in addition to the usually observed peak at $m/z = 1564.6$ $[Cu(L^{1,4})]^+$ with low intensity, an iodide-containing species at $m/z = 1774.1$ assigned as $[Cu_2(L^{1,4})(H_2O)I]^+$, based on its mass and isotopic distribution (Figure S9); formation of this dicopper ion in the ionization chamber is attributed to redistribution of labile Cu(I).

Research Article
doi.org/10.1002/ejic.202200596

The presence of iodide as ligand is supported by addition of AgOTf to an acetonitrile solution of **[Cu(L^{1,4})I]**, which resulted in AgI as a water-insoluble, pale-yellow precipitate. **[Cu(L^{1,4})I]** is EPR silent at X-band frequency, as expected for a diamagnetic d^{10} ion (Figure S10). Finally, combustion analysis is consistent with the formulation as [Cu(**L^{1,4}**)(CH_3CN)(H_2O)I], likely due to the presence of acetonitrile from crystallization (Figure S8) and moisture absorbed during handling in air for analysis.

A separate batch of pale-yellow crystals were obtained by evaporation of a concentrated 9:1 acetonitrile/toluene solution in the triclinic space group *P*-1, and identified as [**Cu(L^{1,4}–H)**(CH_3CN)$_2$] based on X-ray diffraction. However, this species is only a minor product and the bulk of the isolated material corresponds to **[Cu(L^{1,4})I]**, as stated previously and confirmed by combustion analysis, MS, NMR spectroscopy, and reactivity with AgOTf. Hence, the low yield of [**Cu(L^{1,4}–H)**(CH_3CN)$_2$] did not allow us to test its catalytic activity extensively (see below). The crystals lose solvent rapidly once removed from the mother liquor at room temperature, and they diffract poorly despite immediate mounting on a glass capillary under a stream of cold N_2. Nonetheless, careful and rapid handling of the crystals allowed the collection of diffraction data for [**Cu(L^{1,4}–H)**(CH_3CN)$_2$], Figure 1. It consists of a calix[8]arene with the 2,9-dimethylphenanthroyl group bridging the 1 and 4 phenolic positions. One phenolic oxygen donor [O4] is bound to the Cu(I) center, which is chelated by the phenanthroline moiety; its coordination environment is complemented by two acetonitrile molecules as additional N-donors. Notably, the original iodide counterion is absent in these yellow crystals and a deprotonated phenol of the calixarene framework acts as charge compensator. The local geometry of the Cu(I) ion in [**Cu(L^{1,4}–H)**(CH_3CN)$_2$] can be described as a very distorted square pyramid $\tau^5 = 0.228$,[26] with the two phenanthroline N-atoms, O4 and one acetonitrile N-donor at the base of the pyramid, and the second acetonitrile molecule in the apex. The copper-nitrogen bond distances Cu1-N1 and Cu1-N2 (2.064 and 2.079 Å), and the N1-Cu1-N2 angle of 80.0° compare well with related Cu(I) phenanthroline complexes.[27,28] The Cu1-O4 length of 2.746 Å, is shorter than the sum of the van der Waals radii of copper and oxygen (2.9 Å).[29,30] Selected bond lengths (Å) and angles (°) are presented in Table 1. Crystallographic data and structure refinement details are presented in Table S1 in the Supporting Information.

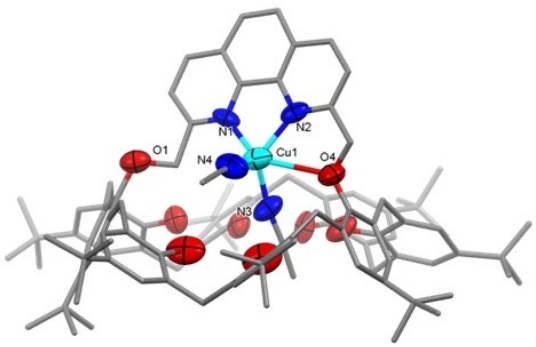

Figure 1. Mercury diagram of [**Cu(L^{1,4}–H)**(CH_3CN)$_2$] (H-atoms and solvent molecules omitted, C-atoms shown as wireframe for clarity). Ellipsoids are presented at the 50% probability level.

The conformation adopted by the substituted calix[8]arene in [**Cu(L^{1,4}–H)**(CH_3CN)$_2$] can be described as 1,2,3,4-alternate, where all phenolic groups are in *syn* orientation.[31] This conformation has been previously observed in calix[8]arene complexes of lanthanides, thorium, and molybdenum, although in all those cases the phenolic oxygen atoms are the only donors present.[32] The arrangement is stabilized by an intramolecular hydrogen-bonding network between the phenolic OH groups, which distributes the anionic charge among the phenol groups. The phenanthroyl bridge connecting the 1 and 4 positions defines a bimacrocyclic calixarene scaffold with an asymmetric cleft composed of a small and a large cycle, integrated by one 23- and one 31-membered rings, respectively. In contrast, the cavity of **L^{1,5}** consists of two symmetric 27-membered rings. For comparative purposes, the small cavity of **L^{1,4}** is only marginally larger than those of calix[4]arene and calix[5]arenes (16- and 20-membered rings), and slightly smaller than that of calix[6]arene (24-membered ring).

Catalytic evaluation. In previous work, **[Cu(L^{1,5})Cl]** had been tested as a catalyst precursor for C–S cross couplings, affording arylthioether products in 70–95% yields with a variety of aryl halides. The activity of this monometallic complex is significantly different from that observed when using small molecular complexes. For example, Bates et al. reported the dimeric complexes [(Me_2phen)Cu(μ-I)]$_2$ and [(Me_2phen)Cu(μ-SC_6H_5)]$_2$ that required 10% mol CuI and 2,9-dimethyl-1,10-phenanthroline (Me_2phen) loads for acceptable catalytic activity.[34] In contrast, the use of 2.5% mol loads of **[Cu(L^{1,5})Cl]** displayed high activity and unusual size-selectivity, demonstrating the influence of the cavity in the process that allows the less hindered substrates to access and interact with the copper center, thus favoring shorter reaction times. For direct comparison, we initially tested the catalytic activity of in situ formed **[Cu(L^{1,4})Cl]** in C–S couplings under analogous reaction conditions, with poor results. Although the difference is only the position of the phenanthroyl moiety, this modifies the size of the cavity, as well as the energetically accessible conformations in solution (see calculations below). Thus, Ullmann-type C–S couplings with the potentially more active iodide complex **[Cu(L^{1,4})I]** as catalyst precursor were carried out following the conditions shown in Scheme 2. We used bromobenzene in initial tests, based on the preference (size-selectivity) over

Table 1. Selected bond lengths (Å) and angles (°) for [**Cu(L^{1,4}–H)**(CH_3CN)$_2$].

Bond lengths		Bond angles	
Cu1-N4	1.944(10)	N4-Cu1-N3	111.6(3)
Cu1-N3	1.987(8)	N4-Cu1-N1	107.5(4)
Cu1-N1	2.064(8)	N3-Cu1-N1	118.2(3)
Cu1-N2	2.079(8)	N4-Cu1-N2	110.0(3)
Cu1-O4	2.746(9)	N1-Cu1-N2	80.0(3)
		O4-Cu1-N2	62.9(2)
		O4-Cu1-N3	75.3(3)
		O4-Cu1-N4	101.1(3)

Research Article
doi.org/10.1002/ejic.202200596

Chemistry Europe
European Chemical Societies Publishing

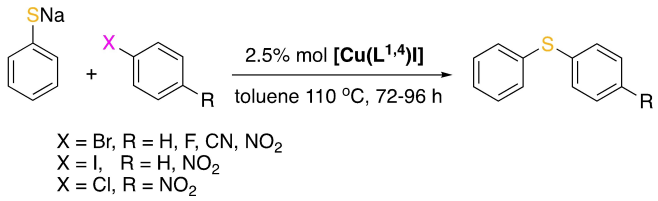

Scheme 2. C–S Ullmann-type couplings with **[Cu(L^{1,4})I]** as catalyst precursor.

iodobenzene exhibited previously by **[Cu(L^{1,5})Cl]**, and the activated 4-fluorobromobenzene, 4-bromobenzonitrile, and 4-nitrobromobenzene (entries 1–4 in Table 1). The catalyst and sodium thiophenolate were suspended in toluene and stirred for an hour, followed by addition of the corresponding arylbromide. The reactions were monitored by TLC analysis at 24 and 72 h intervals, and after such time the mixtures were cooled to room temperature for analysis. The products were separated by column chromatography and isolated or identified whenever necessary by ^{1}H NMR spectroscopy and DART-MS; the yields of isolated coupling product are shown in Table 2. Although the reactions were carried out under inert atmosphere, **[Cu(L^{1,4})I]** can be handled in air, based on EPR analysis of samples of the complex exposed to air for several days (Figure S11). This is attributed to the steric protection of Cu(I) provided by the calixarene scaffold.

Bromobenzene was the first substrate tested, and no cross-coupling product was detected by TLC analysis, even after 72 h of reaction at 110 °C; only reactants and catalyst were observed.

Table 2. Ullmann-type C–S cross-coupling of aryl halides using **[Cu(L^{1,5})Cl]**[a] and **[Cu(L^{1,4})I]**.

Entry	ArX	Product yield [%] **[Cu(L^{1,5})Cl]**[a]	**[Cu(L^{1,4})I]**
1	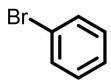	95	0
2	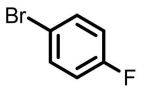	NA	0
3	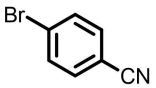	94	Trace
4	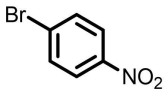	95	35
5		88	0
6	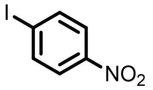	NA	31
7	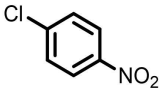	94	19

[a] Previous work from Ref. [23]. NA: Not available.

This was also the case after chromatographic separation. Catalyst recovery was partially successful: although the complex appears to decompose in silica, the ligand was isolated with a maximum of 80% yield. In a few specific cases of the coupling reactions, the copper complex was recovered as well in ca. 30% yield. Unlike copper catalyst with **L^{1,5}**, for which the cross-coupling reaction generates diarylsulfides in 15 h with up to 95% yield, **[Cu(L^{1,4})I]** is not a viable catalyst with the simplest substrate bromobenzene. Therefore, we decided to try substrates with activating (electron withdrawing) groups in the *para* position (F, CN, and NO_2). Even though 4-fluorobromobenzene may be considered as activated relative to bromobenzene, no reaction with sodium thiophenolate was observed. When 4-bromobenzonitrile was employed as substrate, the coupling product was spotted by TLC, ^{1}H NMR studies, and mass spectra analysis (Figures S12 and S13), but this was isolated only in trace amounts. Coupling was successful only with the most highly activated 4-nitrobromobenzene, affording a new compound that was isolated as an intense yellow oil after column chromatography. DART-MS shows a peak corresponding to the desired coupling product (4-nitrophenyl)phenylsulfide at $m/z =$ 232 for $[M+H]^+$ (Figure S14). ^{1}H NMR spectroscopy in Figure S14 confirms the identity of the coupling product, corresponding to 35% yield.

Considering that **[Cu(L^{1,4})I]** requires the most active substituted bromobenzene substrate to perform the coupling reaction, three additional tests were carried out using iodobenzene, 4-nitroiodobenzene and 4-nitrochlorobenzene. These substrates allowed us to evaluate the effect of the size of the halide in reactivity under the same conditions employed with arylbromides. The results of these experiments are summarized in Table 2 entries 5–7. When using iodobenzene, no product could be identified as diphenyl sulfide after column chromatography. Reactions with 4-nitroiodobenzene and 4-nitrochlorobenzene afforded the coupling product (4-nitrophenyl)phenylsulfide, isolated after column chromatography, corresponding to 31% and 19% yields respectively (see DART-MS in Figures S16 and S17). These observations evidence that coupling reactions proceed only when using *highly activated* aryl halides with **[Cu(L^{1,4})I]** as catalyst, albeit in moderate yields. This contrasts with the high activity established for the 1,5-substituted system with all types of substrates, although the size preference for aryl bromides over aryl iodides is retained. The low catalytic activity of **[Cu(L^{1,4})I]** can be ascribed to the difference of the cavity size and shape, and potentially to the conformations that may be accessible for both macrocycles. While in **[Cu(L^{1,5})Cl]** the Cu(I) ion is oriented towards the center of the cavity, allowing the substrates to enter and interact with the metal ion, in **[Cu(L^{1,4})I]** the position of the Cu(I) ion is shifted to one side, restricting the conformations that may lead to high conversions with any arylhalide.

A common phenomenon observed in all reactions tested was that biphenyl was not detected. This supports the notion that in **[Cu(L^{1,4})I]** the space to access the copper center is highly restricted by the conformations available to the calixarene framework. The extent of restriction is such that two aryl halides

Research Article
doi.org/10.1002/ejic.202200596

cannot be fitted simultaneously for homocoupling to take place, regardless of the identity of the halogen substituent on the aromatic substrates. When C–S coupling does occur, the mechanism must be similar to that postulated for these types of systems, where initial formation of Cu(I)-thiophenolate is followed by oxidative addition of the arylhalide, and product formation takes place by reductive elimination in the last step in Scheme 3. As an alternative, if [**Cu(L^{1,4}–H)**(CH$_3$CN)$_2$] were present, the calixarene phenolate moiety (**L^{1,4}–H**) may be protonated by the more acidic thiophenol PhSH, which would lead to [**Cu(L^{1,4})(SPh)**] in Scheme 3; the rest of the mechanism should be identical to the one shown. This catalytic reaction was indeed tested with the small amount of [**Cu(L^{1,4}–H)**(CH$_3$CN)$_2$] available and PhSH/PhBr, with no products observed (see Experimental Section for details).

Computational conformational studies. To shed light on the reasons for the considerably lower activity of **[Cu(L^{1,4})X]** relative to **[Cu(L^{1,5})X]**, a theoretical investigation of the structures was undertaken. Initial structure optimizations with DFT did not show a big difference in energy for the two regioisomeric complexes (**[Cu(L^{1,4})I]** and **[Cu(L^{1,5})I]**, shown in Figure S18), with **[Cu(L^{1,4})I]** being slightly more stable by 10 kJ mol^{-1}. To explore the flexibility of the calixarene macrocycle in solution, we performed accelerated MD (aMD) simulations of **[Cu(L^{1,4})I]** and **[Cu(L^{1,5})I]** in explicit chloroform (see computational methodology for details) — a methodology established in a previous study on a similar system.[35] To quantify the change in conformational flexibility induced by the bridging phenanthroyl moiety at the 1,4 and 1,5 positions, an analysis of the dihedral angles between the individual calixarene phenolic units was performed. Based on their distribution, an estimate for the dihedral entropy as an indicator of inherent flexibility can be obtained via kernel density estimation (see computational details). For a given dihedral distribution, the entropy value can be obtained by analyzing the area under the curve (the larger the area, the higher the entropy). As seen in Figure 2, where the distributions of the individual dihedral angles are plotted for both complexes, the **[Cu(L^{1,4})I]** structures exhibit significantly more flexibility, especially in the larger loop, as evidenced by the higher entropy values.

The MD simulations also revealed an interesting difference in the behavior of the two structures, with **[Cu(L^{1,4})I]** displaying a deformation of the cavity. This is in stark contrast to the symmetric **[Cu(L^{1,5})I]** catalyst. As depicted in Figure 3 (full structures in Figure S19 and S20), the catalytic center becomes exposed to solvent as the framework deforms. Transition from the deformed to the intact cavity happens several times over the course of a single 1 μs aMD simulation, as well as during the 100 ns conventional MD simulation used to obtain the aMD parameters (see computational details). Upon optimization of the cluster representatives of the two distinct conformations with DFT, it is evident that the deformed structure is slightly more stable than the intact one ($\Delta E = -10$ kJ mol^{-1}). These findings provide evidence that the deformation of the cavity is likely to occur under experimental conditions and may explain the low catalytic activity of **[Cu(L^{1,4})I]** relative to **[Cu(L^{1,5})I]**. Although the deformed calculated structures suggest that dimerization might be feasible, no experimental evidence for deactivation through Cu–I–Cu bridge formation, i.e. dimerization, was found. If the reaction were to proceed in the

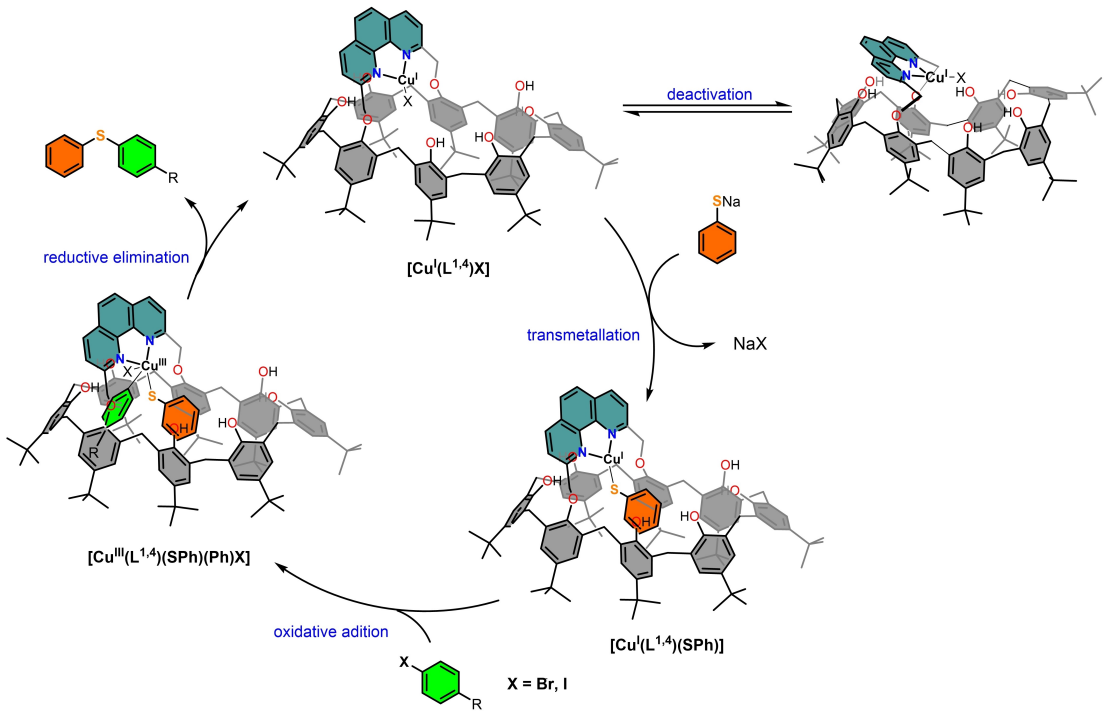

Scheme 3. Proposed mechanism for the (inefficient) C–S cross coupling of thiophenolate with aryl halides using **[Cu(L^{1,4})I]** as catalyst, including potential deactivation pathway.

Research Article
doi.org/10.1002/ejic.202200596

Chemistry Europe
European Chemical Societies Publishing

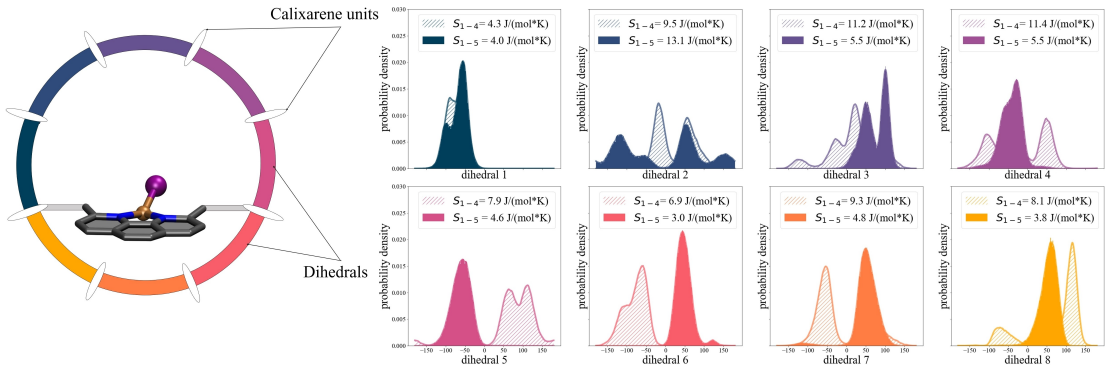

Figure 2. Left: schematic representation of **[Cu(L^{1,4})I]** depicting the position of each dihedral angle. Right: dihedral entropy estimated from the area under the curve of **[Cu(L^{1,4})I]** (patterned curves) and **[Cu(L^{1,5})I]** (filled curves) as observed during aMD simulations.

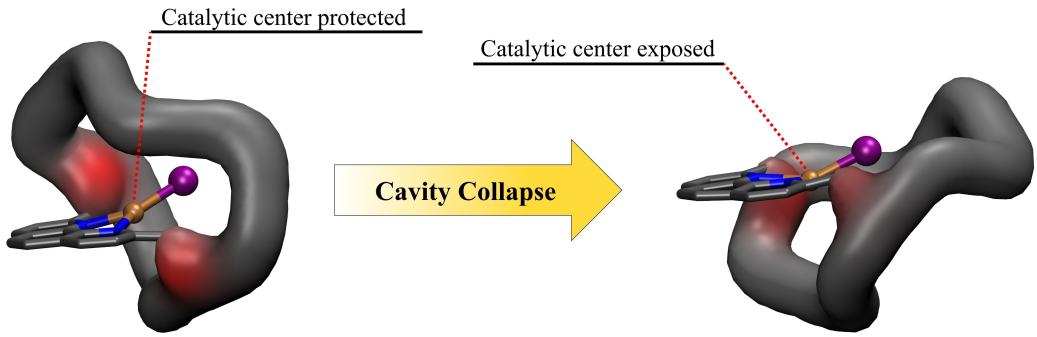

Figure 3. Schematic representation of the intact and deformed structures of **[Cu(L^{1,4})I]** observed during the aMD simulations in explicit solvent. The calixarene macrocycle is displayed as wiggle. Left: front and side views of the intact conformation; right: deformed structure with exposed Cu(I) center. Detailed structures shown in Figures S17 and S18 in the Supporting Information.

deformed conformation with an exposed catalytic center, replacement of iodide for thiophenolate would require more open space around the Cu center. The transmetallation is a two-step process, wherein a bulky, negatively charged intermediate, **[Cu(L^{1,4})I(SPh)]$^-$**, would be formed upon the addition of thiophenolate. This would be followed by the dissociation of iodide, resulting in **[Cu(L^{1,4})(SPh)]** (Scheme 3). To investigate the first step of the transmetallation, we modelled the intermediate as **[Cu(L^{1,4})I(SPh)]$^-$Na$^+$** to balance the charge in the simulation (see computational methodology for details). Given that thiophenolate is added as a sodium salt and that the solvent is non polar, it is reasonable to assume that the Na^+ remains in the vicinity of the negatively charged **[Cu(L^{1,4})I(SPh)]$^-$** complex. Our aMD simulations performed on the **[Cu(L^{1,4})I(SPh)]$^-$Na$^+$** intermediate, revealed a preference for the deformed structure. This finding supports the hypothesis that the large steric demand of the intermediate prevents the calixarene from flipping back to its original position and restoring the cavity. Indeed, the starting structure transitioned to a deformed one within the 100 ns conventional MD simulation. Transitions between conformations are rare in a 1 μs simulation, where only 2.2% of the structures show an intact cage. Moreover, a simple experimental transmetallation test between **[Cu(L^{1,4})I]** and NaSPh at room temperature did not afford evidence of the formation of **[Cu(L^{1,4})(SPh)]** by MALDI-TOF MS. Re-optimization of the deformed **[Cu(L^{1,4})I(SPh)]$^-$Na$^+$** structures, obtained from MD simulations after clustering of the trajectory, with DFT revealed that these very compact conformations (see Figures S21–S22) are surprisingly stable. In fact, the deformed structure is 165 kJ mol^{-1} more stable than that with an intact cage. This finding is in line with results from MD simulations, where the intact cage conformation was hardly populated. Attempts to optimize the subsequent putative reactive intermediate **[Cu(L^{1,4})X(SPh)(Ph)]** (X=Br, I), proposed in Scheme 3 failed, with the calculations directly leading to the formation of the C–S coupling product (see Figure S23). This result suggests that sterically demanding species are not stable within the coordination environment of **[Cu(L^{1,4})I]**. This means either the oxidative addition cannot take place, or it is immediately followed by reductive elimination. In any case, the computational investigations highlight the importance of the 1,5-substitution pattern of **L^{1,5}** to preserve a reaction cavity that results in high catalytic activity, allowing the reaction to

Research Article
doi.org/10.1002/ejic.202200596

proceed via the known oxidative addition/reductive elimination pathway.

Conclusion

We have successfully isolated and characterized the 1,4-regioisomer of *p-tert*-butylcalix[8]arene substituted with a phenanthroyl moiety $\mathbf{L^{1,4}}$ by easy separation of the cesium complex of $\mathbf{L^{1,5}}$ via crystallization. $\mathbf{L^{1,4}}$ was employed as ligand to obtain the new copper(I) complex **[Cu($\mathbf{L^{1,4}}$)I]**. Spectroscopic studies and structure optimization of **[Cu($\mathbf{L^{1,4}}$)I]** by theoretical methods evidenced that the asymmetric cleft provided by $\mathbf{L^{1,4}}$ forces Cu(I) towards one side of the calixarene framework, relative to its symmetric **[Cu($\mathbf{L^{1,5}}$)I]** counterpart. Catalytic C–S cross-coupling reactions of sodium thiophenolate with different aryl halides and **[Cu($\mathbf{L^{1,4}}$)I]** as catalyst were tested. Product formation only occurs when highly activated 4-nitroaryl halides were used, although the yields obtained reached only a maximum value of 35 % despite extended reaction times. The computational investigation of the two regioisomers delivers new insights into the conformational dynamics that can affect supramolecular catalytic activity. The high flexibility of the asymmetric cage resulted in a deformation of the calix[8]arene structure in **[Cu($\mathbf{L^{1,4}}$)I]** that is likely the cause for the low catalytic activity. Our studies highlight the importance of the conformational landscape available for inherently flexible macrocycles, particularly when aimed at providing a reactive pocket for catalytic transformations. X-ray diffraction studies of the minor product **[Cu($\mathbf{L^{1,4}}$–H)**$(CH_3CN)_2]$ confirm the nature of the 1,4-isomer, as well as the rare *endo*-oriented coordination of the metal center.[17] Studies with different transition-metal ions hosted within $\mathbf{L^{1,4}}$ and $\mathbf{L^{1,5}}$ to further explore their properties are currently underway.

Experimental Section

Materials and methods: All preparations and manipulations of air sensitive compounds were carried out under dinitrogen atmosphere using an MBraun glovebox or standard Schlenk techniques. Copper iodide (CuI), sodium thiophenolate ($NaSC_6H_5$), bromobenzene (C_6H_5Br), 4-fluorobromobenzene (BrC_6H_4F), 4-bromobenzonitrile (BrC_6H_4CN), 4-nitrobromobenzene ($BrC_6H_4NO_2$), iodobenzene (IC_6H_5), 4-nitroiodobenzene ($IC_6H_4NO_2$) and 4-nitrochlorobenzene ($ClC_6H_4NO_2$) were purchased from Sigma-Aldrich and used without further purification. Toluene (Sigma-Aldrich, 99.5 %) was dried over Na/benzophenone, distilled under N_2, and degassed via three freeze-pump-thaw cycles.[36] ^{1}H NMR spectra were recorded on a JEOL Eclipse spectrometer operating at 300 MHz and referenced to the residual solvent signal of $C_2D_2Cl_4$ (s, $\delta = 6.0$ ppm). MALDI-TOF MS were acquired with a Bruker Microflex MALDI-TOF mass spectrometer using a 2,5-dihydroxybenzoic acid matrix. ATR-IR spectra were recorded on a Frontier Perkin Elmer FTIR spectrometer. EPR spectra were acquired in quartz tubes with a JEOL JES TE300 spectrometer operating at X-band frequency (9.4 GHz) at 100 KHz field modulation, with a cylindrical cavity (TE011 mode). Thin layer chromatography (TLC) was conducted using aluminum-backed TLC Silica Gel 60 F_{254}. A mixture of hexane/acetone 3 : 1 was used as eluant. Visualization of developed plates was performed under UV-vis light (245 nm) or with an iodine chamber. Retardation factors (R_F) were calculated as recommended by IUPAC.[37] Column chromatography was performed using 70–230 mm silica gel as stationary phase and hexane as eluant.

Crystallographic details: Due to the high instability of single crystals of **[Cu($\mathbf{L^{1,4}}$–H)**$(CH_3CN)_2]$, several crystals had to be tested. A suitable single crystal was mounted on a glass fiber; crystallographic data were collected with an Oxford Diffraction Gemini "A" diffractometer with a CCD area detector, with $\lambda_{Mo K\alpha} = 0.71073$ Å at 170 K. Unit cell parameters were determined with a set of three runs of 15 frames (1° in ω). The double pass method of scanning was used to exclude any noise.[38] The collected frames were integrated by using an orientation matrix determined from the narrow frame scans. Final cell constants were determined by a global refinement; collected data were corrected for absorbance by using analytical numeric absorption correction using a multifaceted crystal model based on expressions upon the Laue symmetry with equivalent reflections. Structures solutions and refinement were carried out with the SHELXS-2014[39] and SHELXL-2014[40] packages. WinGX v2018.[41] software was used to prepare material for publication. Full-matrix least-squares refinement was carried out by minimizing $(Fo^2–Fc^2)^2$. All non-hydrogen atoms were refined anisotropically. H atoms attached to C atoms were placed in geometrically idealized positions and refined as riding on their parent atoms, with C–H = 0.95–0.99 Å and with $U_{iso}(H) = 1.2U_{eq}(C)$ for aromatic and methylene groups, and $1.5U_{eq}(C)$ for methyl groups. The *tert*-butyl groups located on C20, C31, C53, C75 and C97 are disordered. On the other hand, the solvent molecules were significantly disordered and could not be modelled properly, thus SQUEEZE,[42] a part of the PLATON package of crystallographic software, was used to calculate the solvents disorder areas and remove their contributions to the overall intensity data. The disordered solvent area is centered on the 0.084 0.411 0.428 position and showed an estimated total of 127 electrons and a void volume of 2271 Å^3. Crystallographic data for the complex is presented in Table S1 of the Supporting Information.

Deposition Number(s) 1441364 contain(s) the supplementary crystallographic data for this paper. These data are provided free of charge by the joint Cambridge Crystallographic Data Centre and Fachinformationszentrum Karlsruhe Access Structures service.

Synthesis of $\mathbf{L^{1,4}}$ and $\mathbf{L^{1,5}}$: *p-tert*-butylcalix[8]arene (1.45 g, 0.91 mmol) and CsF (1.38 g, 9.1 mmol) were dried for two hours at 120 °C under vacuum. After allowing to cool to room temperature, anhydrous THF was added, and the mixture was heated to reflux for 4 h. Upon cooling to room temperature, 2,9-bis(bromomethyl)-1,10-phenanthroline (400 mg, 1.09 mmol) was added to the mixture and stirred for 36 h. The solvent was then evaporated under reduced pressure to afford a yellow solid that was dissolved in a $CHCl_3$/toluene 8 : 1 mixture and placed in a −30 °C freezer until a white precipitate appeared after 3–4 days. The solid was filtered to remove **[Cs($\mathbf{L^{1,5}}$–H)]** (41 % yield of $\mathbf{L^{1,5}}$ after neutralization) and the solution containing **[Cs($\mathbf{L^{1,4}}$–H)]** was washed with 50 mL of HCl (0.1 M) to remove cesium as CsCl, and then washed with a saturated solution of $NaHCO_3$ for neutralization, affording $\mathbf{L^{1,4}}$ in 46 % yield; m. p. = 200–202 °C (dec). IR (ATR) n (cm^{-1}) = 2959 (C–H), 1594 (C=N), 1481 (C=C). MALDI-TOF MS *m/z*: 1501 $[\mathbf{L^{1,4}} + H]^+$. ^{1}H NMR ($C_2D_2Cl_4$, 300 MHz): δ 9.53 (s, 6H, OH), 8.42 (d, J = 8.03 Hz, 2H Ar_{phen}), 7.91 (m, 2H, Ar_{phen}), 7.81 (s, 2H, Ar_{phen}), 7.21 (m, 16H, Ar_{calix}), 5.53 (m, 2H, $–CH_2$-$_{phen}$), 5.17 (s, 2H, $–CH_2$-$_{phen}$), 4.43 (m, 4H, $–CH_2$-$_{calix}$), 4.10 (m, (8H, $–CH_2$-$_{calix}$), 3.63 (m, (4H, $–CH_2$-$_{calix}$), 1.40-1.30 (m, 72H, ^{t}–Bu). Elemental analysis for $C_{103.5}H_{123.5}ClN_{2.5}O_{8.5}$ **[$\mathbf{L^{1,4}}$**$(0.5CH_3CN, 0.5CH_2Cl_2, 0.5H_2O)]$ calcd.: C 78.98, H 7.91, N 2.22; found: C 78.70, H 7.62, N 2.11.

Research Article
doi.org/10.1002/ejic.202200596

Synthesis of [Cu($L^{1,4}$)I]: To a solution of $L^{1,4}$ (390 mg, 0.26 mmol) in 5 mL of anhydrous, and deoxygenated toluene inside a glovebox was added CuI (49 mg, 0.26 mmol). The brown solution was stirred at room temperature overnight. Toluene was then evaporated under reduced pressure to afford a brown solid that was dissolved in an acetonitrile/toluene 9:1 mixture. Slow evaporation afforded a small amount of yellow crystals (<5% [Cu($L^{1,4}$–H)($CH_3CN)_2$]) that were collected for X-ray diffraction; elemental analysis for $C_{104}H_{124}CuN_3O_9$ [Cu($L^{1,4}$–H)(CH_3CN)(H_2O)] calcd.: C 76.93, H 7.70, N 2.59; found: C 76.90, H 7.46, N 2.73. The remaining solution was placed in a −30 °C freezer, resulting in a brown microcrystalline solid (360 mg, 82% yield); m. p. = 170–172 °C (dec). IR ATR ν (cm^{-1}) = 2954 (C–H), 1591 (C=N), 1481 (C=C). MALDI-TOF MS *m/z*: 1564 [Cu($L^{1,4}$)]$^+$. ^{1}H NMR ($C_2D_2Cl_4$, 300 MHz): δ 9.17 (s, 1H, OH), 8.56 (d, J = 8.0 Hz, 2H Ar_{phen}), 8.31 (s, 2H, Ar_{phen}), 7.94 (m, 2H, Ar_{phen}), 6.98 (m, 16H, Ar_{calix}), 6.50 (d, J = 16.1 Hz, 2H, $-CH_2$-$_{phen}$), 5.82 (d, J = 16.1 Hz, 2H, $-CH_2$-$_{phen}$), 4.69 (d, J = 12.8 Hz, 2H, $-CH_2$-$_{calix}$), 4.35 (d, J = 12.4 Hz, 2H, $-CH_2$-$_{calix}$), 4.15 (d, J = 13.4 Hz, 2H, $-CH_2$-$_{calix}$), 3.93 (d, J = 15.7 Hz, 2H, $-CH_2$-$_{calix}$), 3.78 (d, J = 15.0 Hz, 2H, –CH2-$_{calix}$), 3.61 (d, J = 12.9 Hz, 2H, $-CH_2$-$_{calix}$), 3.53 (d, J = 14.6 Hz, 4H, $-CH_2$-$_{calix}$), 1.37 (s, 9H, ^{t}–Bu), 1.30 (s, 18H, ^{t}–Bu), 1.26 (s, 24H, ^{t}–Bu), 1.23 (s, 24H, ^{t}–Bu), 1.07 (s, 24H, ^{t}–Bu). Elemental analysis for $C_{104}H_{127}Cl_2CuIN_3O_{10}$ [Cu($L^{1,4}$)(CH_3CN)($2H_2O$)$_2$I] calcd.: C 70.59, H 7.23, N 2.37; found: C 70.39, H 6.99, N 2.38.

Coupling reactions: In a typical procedure, sodium thiophenolate (93 mg, 0.71 mmol) was added to a solution of **[Cu($L^{1,4}$)I]** (30 mg, 2.5% mol) in 5 mL of anhydrous toluene in a 100 mL Schlenk flask under dinitrogen atmosphere, the mixture was stirred for 1 h at room temperature followed by the addition of 0.71 mmol of the corresponding aryl bromide. The mixture was heated to 110 °C for 24–72 h. An analogous test was run with 30 mg [Cu($L^{1,4}$–H)($CH_3CN)_2$], 0.71 mmol thiophenol and 0.71 mmol bromobenzene; this resulted in no detectable products, as judged in all cases by TLC analysis on silica gel; final products when present were purified and isolated after column chromatography with hexanes/dichloromethane gradient (starting with 100% hexanes) as eluant.

Quantum chemical studies: The initial geometries of **[Cu($L^{1,4}$)I]** and **[Cu($L^{1,5}$)I]** for the optimizations were constructed by modification of available crystal structures using Chemcraft 1.8.[43] Quantum chemical calculations were performed with Turbomole 7.5,[44] unless otherwise specified. All investigated structures were fully optimized using the PBE0[45] functional and def2-SVP[46] basis set with empirical dispersion corrections of the D3 type,[47] along with implicit solvent corrections using the Conductor-Like Screening Model (COSMO).[48] A dielectric constant of ε = 2.4 was chosen to model toluene. The PBE0 functional is known to provide good results when investigating structures involving transition metals.[49,50] To obtain more accurate electronic energies, the def2-TZVP basis set[46,51–54] was used, alongside the same settings as mentioned above. The minima were verified to be true by running numerical frequency calculations which were then checked for the absence of imaginary frequencies.

Molecular dynamics simulations: Obtaining a representative structural ensemble of the calixarene required that the conformational spaces of these two species are examined along the reaction pathway, for both the $L^{1,4}$ and the $L^{1,5}$ type of structures, by selecting several intermediates. The exploration of the potential energy surface was done using classical accelerated MD simulations, a method proven to deliver reliable conformational ensembles for macrocycles.[20] Sampling in explicit solvent proved to be essential to retain intact cavities, as attempts in implicit solvent resulted in the cavity collapsing upon itself. Test calculations on **[Cu($L^{1,5}$)I]** have shown that there is no significant difference whether chloroform or toluene was used.[35] To this end, chloroform was picked as the explicit solvent of choice, due to a faster equilibration. We chose to simulate the supramolecular structures **[Cu($L^{1,4}$)I]** and **[Cu($L^{1,5}$)I]**, to assess how the flexibility of the cavity changes depending on the position of the bridge. We also simulated the intermediate **[Cu($L^{1,4}$)I(SPh)]$^-$Na$^+$**, which is the first species to be formed in the transmetallation process.[35] Therefore, a parametrization of the metal at the center of the molecule was required. MCPB.py[55] was selected as the tool of choice for the parametrization step. The structure optimizations and frequency calculations for the metal center parametrization were performed at the PBE0/def2-SVP/D3 level. **[Cu($L^{1,4}$)I(SPh)]$^-$Na$^+$** was simulated using Na^+ as an explicit counterion to reduce the net charge of the system to 0. This is in line with experimental conditions, where thiophenolate was added as a sodium salt.

To perform the initial equilibrations prior to simulation production runs, a modified procedure by Wallnöfer et al.[56] that involves extensive heating and cooling was employed. The production runs (in explicit chloroform) were carried out in NpT ensembles at 300 K, using Amber20.[57] The temperature was regulated with the Langevin thermostat,[58] and the pressure was kept at 1 bar using the Berendsen barostat.[59] The SHAKE algorithm[60] was used to restrain hydrogen bonds allowing for a time step of 2 fs; coordinates were saved every 10 ps, simulating a total of 1 μs. Accelerated MD simulations were carried out using the dual-boost algorithm implemented in Amber20, where a bias was applied on the total potential and an additional boost on the dihedral term. Several aMD simulations, each with 1μs were performed with various boosting parameters. These settings were derived by performing 100 ns classical MD simulations, as proposed by Pierce et al.[61] The obtained structures were aligned on the phenanthroyl bridge. A hierarchical clustering was applied on the trajectories to obtain a structurally diverse ensemble. The reweighting of the aMD simulations was not necessary, as the energetics were not a concern, since we aimed at obtaining a large conformational ensemble, from which representative structures were selected and further optimized with DFT. To investigate the flexibility of the calixarene units, a dihedral analysis was used, to characterize the rotations between each moiety. Dihedral angles were assigned between the planes of each of the 6-membered rings of the calixarene units, as changes in these angles accurately describe the movements within the calixarene ring. The relative entropy values were obtained by using the X-entropy[62] script that performs an entropic analysis on the angle distributions by kernel density estimation. Thus, it leads to an accurate estimation of the flexibility, whereby the more flexible the system, the larger the area under the dihedral distribution curve, and the larger the entropy. DFT calculations on the cluster representatives or structure optimizations were performed with the protocol described in the previous section. Structural parameter measurements and visualizations were done with PyMol and VMD.[63,64]

Acknowledgements

The authors thank María del Carmen García-González for DART-MS, Lucero Ríos-Ruiz for MALDI-TOF, Virginia Gómez-Vidales for EPR measurements, María de los Angeles Peña for NMR spectroscopy, and María de la Paz Orta for combustion analysis. A. B.-V., C. R.-M. and I. C. thank Instituto de Química, UNAM, and Conacyt (Becas 736348, 308307), Proyecto A1-S-8682 for financial support. M. P. thanks the FWF for financial support (P 33528).

Conflict of Interest

The authors declare no conflict of interest.

Data Availability Statement

The data that support the findings of this study are available in the supplementary material of this article. Calculated structures are deposited at https://zenodo.org/record/7444229.

Keywords: Calixarenes · Conformational sampling · Copper · DFT calculations · Macrocycles

[1] T. Chavagnan, D. Sémeril, D. Matt, L. Toupet, *Eur. J. Org. Chem.* **2017**, *2017*, 313–323.
[2] H. Zhou, J. Tan, X. Zhang, *Chem. Asian J.* **2019**, *14*, 3240–3250.
[3] V. Mouarrawis, R. Plessius, J. I. van der Vlugt, J. N. H. Reek, *Front. Chem.* **2018**, *6*, 623.
[4] L. Leclercq, G. Douyère, V. Nardello-Rataj, *Catalysts* **2019**, *9*, 163.
[5] C. Deraedt, D. Astruc, *Coord. Chem. Rev.* **2016**, *324*, 106–122.
[6] C. Schöttle, E. Guan, A. Okrut, N. A. Grosso-Giordano, A. Palermo, A. Solovyov, B. C. Gates, A. Katz, *J. Am. Chem. Soc.* **2019**, *141*, 4010–4015.
[7] P. Molenveld, J. F. J. Engbersen, D. N. Reinhoudt, *Chem. Soc. Rev.* **2000**, *29*, 75–86.
[8] C. Dieleman, S. Steyer, C. Jeunesse, D. Matt, *J. Chem. Soc. Dalton Trans.* **2001**, 2508–2517.
[9] E. Karakhanov, T. Buchneva, A. Maximov, M. Zavertyaeva, *J. Mol. Catal. A* **2002**, *184*, 11–17.
[10] Z. X. Xu, G. K. Li, C. F. Chen, Z. T. Huang, *Tetrahedron* **2008**, *64*, 8668–8675.
[11] I. Di Bari, G. Granata, G. M. L. Consoli, S. Sortino, *New J. Chem.* **2018**, *42*, 18096–18101.
[12] X. Hang, W. Yang, S. Wang, H. Han, W. Liao, J. Jia, *ACS Appl. Nano Mater.* **2019**, *2*, 4232–4237.
[13] N. Noll, F. Würthner, *Chem. Eur. J.* **2021**, *27*, 444–450.
[14] A. Labattut, S. Abi Fayssal, J. Buendia, I. Abdellah, V. Huc, C. Martini, E. Schulz, *React. Chem. Eng.* **2020**, *5*, 1509–1514.
[15] N. Narkhede, B. Uttam, C. P. Rao, *ACS Omega* **2019**, *4*, 4908–4917.
[16] S. Abi Fayssal, T. Naret, V. Huc, J. Buendia, C. Martini, E. Schulz, *Catal. Sci. Technol.* **2021**, *11*, 5223–5231.
[17] C.-G. Yan, J. Han, L. Li, D.-M. Liu, *J. Coord. Chem.* **2009**, *62*, 825–832.
[18] N. Le Poul, Y. Le Mest, I. Jabin, O. Reinaud, *Acc. Chem. Res.* **2015**, *48*,2097–2106.
[19] G. Izzet, J. Zeitouny, H. Akdas-Killig, Y. Frapart, S. Ménage, B. Douziech, I. Jabin, Y. Le Mest, O. Reinaud, *J. Am. Chem. Soc.* **2008**, *130*, 9514–9523.
[20] V. Böhmer, *Angew. Chem. Int. Ed.* **1995**, *34*, 713–745.
[21] G. M. L. Consoli, F. Cunsolo, C. Geraci, P. Neri, *Org. Lett.* **2001**, *3*, 1605–1608.
[22] C. Gaeta, L. Gregoli, M. Martino, P. Neri, *Tetrahedron Lett.* **2002**, *43*, 8875–8878.
[23] E. Guzmán-Percástegui, D. J. Hernández, I. Castillo, *Chem. Commun.* **2016**, *52*, 3111–3114.
[24] R. H. Crabtree, *Chem. Rev.* **2015**, *115*, 127–150.
[25] D. J. Hernández, H. Vázquez-Lima, P. Guadarrama, D. Martínez-Otero, I. Castillo, *Tetrahedron Lett.* **2013**, *54*, 4930–4933.
[26] A. W. Addison, T. N. Rao, J. Reedijk, J. Van Rijn, G. C. Verschoor, *J. Chem. Soc. Dalton Trans.* **1984**, 1349–1356.
[27] J. Cody, J. Dennisson, J. Gilmore, D. G. VanDerveer, M. M. Henary, A. Gabrielli, C. D. Sherrill, Y. Zhang, C. P. Pan, C. Burda, C. J. Fahrni, *Inorg. Chem.* **2003**, *42*, 4918–4929.
[28] C. Chen, Z. Weng, J. F. Hartwig, *Organometallics* **2012**, *31*, 8031–8037.
[29] S. S. Batsanov, *Inorg. Mater.* **2001**, *37*, 871–885.
[30] A. O. Legendre, F. C. Andrade, S. R. Ananias, A. E. Mauro, A. V. G. Netto, R. H. A. Santos, J. G. Ferreira, F. R. Martins, *J. Braz. Chem. Soc.* **2006**, *17*, 1683–1688.
[31] P. R. Martínez-Alanis, I. Castillo, *Tetrahedron Lett.* **2005**, *46*, 8845–8848.
[32] C. D. Gutsche, *Calixarenes Revisited*, Royal Society Of Chemistry, **1998**.
[33] K. Nakamoto, *Infrared and Raman Spectra of Inorganic and Coordination Compounds*, John Wiley & Sons, Inc., Hoboken, NJ, USA, **2008**.
[34] C. G. Bates, R. K. Gujadhur, D. Venkataraman, *Org. Lett.* **2002**, *4*, 2803–2806.
[35] R. A. Talmazan, R. Monroy, F. del Río-Portilla, I. Castillo, M. Podewitz, *ChemCatChem* **2022**, e202200662.
[36] G. Luyckx, J. Ceulemans, *Bull. Soc. Chim. Belg.* **1987**, *96*, 151–163.
[37] L. S. Ettre, *Pure Appl. Chem.* **1993**, *65*, 819–872.
[38] CrysAlisPro, *version 1.171.36.32; Oxford Diffr. Ltd. Abingdon, U. K.* **2013**.
[39] G. M. Sheldrick, *Acta Crystallogr. Sect. A* **2015**, *71*, 3–8.
[40] G. M. Sheldrick, *Acta Crystallogr. Sect. C* **2015**, *71*, 3–8.
[41] L. J. Farrugia, *J. Appl. Crystallogr.* **2012**, *45*, 849–854.
[42] A. L. Spek, *Acta Crystallogr. Sect. C* **2015**, *71*, 9–18.
[43] G. A. Zhurko, D. A. Zhurko, Chemcraft. Version 1.8 (Build 610b). www.chemcraftprog.com.
[44] TURBOMOLE V7.5 **2021**, a) development of the University of Karlsruhe and Forschungszentrum Karlsruhe GmnH, *TURBOMOLE*.
[45] C. Adamo, V. Barone, *J. Chem. Phys.* **1999**, *110*, 6158–6170.
[46] F. Weigend, R. Ahlrichs, *Phys. Chem. Chem. Phys.* **2005**, *7*, **3297–3305**.
[47] S. Grimme, S. Ehrlich, L. Goerigk, *J. Comput. Chem.* **2011**, *32*, 1456–1465.
[48] A. Schäfer, A. Klamt, D. Sattel, J. Lohrenz, F. Eckert, *Phys. Chem. Chem. Phys.* **2000**, *2*, 2187–2193.
[49] S. K. Goetzfried, C. M. Gallati, M. Cziferszky, R. A. Talmazan, K. Wurst, K. R. Liedl, M. Podewitz, R. Gust, *Inorg. Chem.* **2020**, *59*, 15312–15323.
[50] M. M. Islam, H. Tomiyasu, T. Matsumoto, J. Tanaka, P. E. Georghiou, C. Redshaw, T. Yamato, *Org. Biomol. Chem.* **2015**, *13*, 9055–9064.
[51] F. Weigend, M. Häser, H. Patzelt, R. Ahlrichs, *Chem. Phys. Lett.* **1998**, *294*, 143–152.
[52] K. Eichkorn, O. Treutler, H. Öhm, M. Häser, R. Ahlrichs, *Chem. Phys. Lett.* **1995**, *240*, 283–289.
[53] K. Eichkorn, F. Weigend, O. Treutler, R. Ahlrichs, *Theor. Chem. Acc.* **1997**, *97*, 119–124.
[54] R. Ahlrichs, *Phys. Chem. Chem. Phys.* **2004**, *6*, 5119–5121.
[55] P. Li, K. M. Merz, *J. Chem. Inf. Model.* **2016**, *56*, 599–604.
[56] H. Wallnöefer, S. Handschuh, K. R. Liedl, T. Fox, *J. Phys. Chem. B.* **2010**, *114*, 7405–7412.
[57] D. A. Case, H. M. Aktulga, K. Belfon, I. Y. Ben-Shalom, S. R. Brozell, D. S. Cerutti, T. E. Cheatham, III, G. A. Cisneros, V. W. D. Cruzeiro, T. A. Darden, R. E. Duke, G. Giambasu, M. K. Gilson, H. Gohlke, A. W. Goetz, R. Harris, S. Izadi, S. A. Izmailov, C. Jin, K. Kasavajhala, M. C. Kaymak, E. King, A. Kovalenko, T. Kurtzman, T. S. Lee, S. LeGrand, P. Li, C. Lin, J. Liu, T. Luchko, R. Luo, M. Machado, V. Man, M. Manathunga, K. M. Merz, Y. Miao, O. Mikhailovskii, G. Monard, H. Nguyen, K. A. O'Hearn, A. Onufriev, F. Pan, S. Pantano, R. Qi, A. Rahnamoun, D. R. Roe, A. Roitberg, C. Sagui, S. Schott-Verdugo, J. Shen, C. L. Simmerling, N. R. Skrynnikov, J. Smith, J. Swails, R. C. Walker, J. Wang, H. Wei, R. M. Wolf, X. Wu, Y. Xue, D. M. York, S. Zhao, P. A. Kollman. Amber **2021**, University of California, San Francisco.
[58] S. A. Adelman, J. D. Doll, *J. Chem. Phys.* **1976**, *64*, 2375–2388.
[59] H. J. C. Berendsen, J. P. M. Postma, W. F. van Gunsteren, A. DiNola, J. R. Haak, *J. Chem. Phys.* **1984**, *81*, 3684–3690.
[60] G. Ciccotti, J. P. Ryckaert, *Comput. Phys. Rep.* **1986**, *4*, 346–392.
[61] L. C. T. Pierce, R. Salomon-Ferrer, C. A. F. de Oliveira, J. A. McCammon, R. C. Walker, *J. Chem. Theory Comput.* **2012**, *8*, 2997–3002.
[62] J. Kraml, F. Hofer, P. K. Quoika, A. S. Kamenik, K. R. Liedl, *J. Chem. Inf. Model.* **2021**, *61*, 1533–1538.
[63] L. Schrodinger, The PyMOL Molecular Graphics System. **2015**.
[64] W. Humphrey, A. Dalke, K. Schulten, *J. Molec. Graphics* **1994**, *14*, 33–38.

Manuscript received: September 21, 2022
Revised manuscript received: November 14, 2022
Accepted manuscript online: December 2, 2022

Corrections added on December, 28 2022, after first online publication: addition of 1) VMD in the last sentence of the Experimental Part, together with the corresponding reference [64]; 2) the link to the repository in the Data Availability Statement.